Physica D 275 (2014) 54–66

Contents lists available at ScienceDirect

Physica D

journal homepage: www.elsevier.com/locate/physd

Nonlinear day-to-day traffic dynamics with driver experience delay: Modeling, stability and bifurcation analysis

Xiaomei Zhao [a,b], Gábor Orosz [c,*]

[a] School of Traffic and Transportation, Beijing Jiaotong University, Beijing, 100044, China

[b] MOE Key Laboratory for Urban Transportation Complex Systems Theory and Technology, Beijing Jiaotong University, Beijing, 100044, China

[c] Department of Mechanical Engineering, University of Michigan, Ann Arbor, MI 48109, USA

HIGHLIGHTS

- Time delays and nonlinearities are introduced into day-to-day traffic models.
- The linear and nonlinear stability of the equilibrium is analyzed.
- Normal forms are derived for the Flip and Neimark–Sacker bifurcations.
- Domains of bistability are determined by numerical continuation.
- Delays extend the bistable region and increase the period of oscillations.

GRAPHICAL ABSTRACT

Day-to-day updating rules for cost and flow with driver experience delay τ:

$$\mathbf{c}_{t+1} = \alpha\, C(\mathbf{f}_{t-\tau}) + (1-\alpha)\,\mathbf{c}_t\,,$$
$$\mathbf{f}_{t+1} = \beta\, F(\mathbf{c}_{t+1}) + (1-\beta)\,\mathbf{f}_t\,.$$

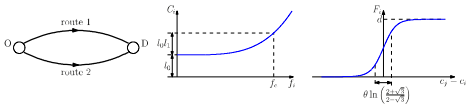

Figure 1: **Left**: a two-route traffic network. **Middle**: nonlinear cost function. **Right**: network loading function.

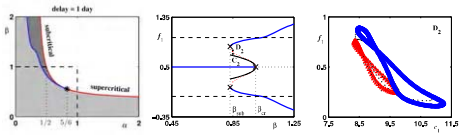

Figure 2: **Left**: global stability chart with linearly stable (light gray), bistable (dark gray), and unstable (white) domains. **Middle**: bifurcation diagram for $\alpha = 1/2$ with subcritical Neimark-Sacker bifurcation. **Right**: stable and unstable tori in state space.

ARTICLE INFO

Article history:
Received 26 April 2013
Received in revised form
28 November 2013
Accepted 7 February 2014
Available online 19 February 2014
Communicated by G. Stepan

Keywords:
Day-to-day traffic models
Driver experience delay
Subcritical Neimark–Sacker bifurcation
Normal forms
Numerical continuation
Bistability

ABSTRACT

In day-to-day traffic assignment problems travelers' past experiences have important impact on their cost prediction which influences their route choice and consequently the arising flow patterns in the network. Many travelers execute the same trip in every few days, not daily, which leads to time delays in the system. In this paper, we propose a nonlinear, discrete-time model with driver experience delay. The linear stability of the stochastic user equilibrium is analyzed by studying the eigenvalues of the Jacobian matrix of the system while the nonlinear oscillations arising at the bifurcations are investigated by normal form calculations, numerical continuation and simulation. The methods are demonstrated on a two-route example. By applying rigorous analysis we show that the linearly unstable parameter domain as well as the period of arising oscillations increase with the delay. Moreover, delays and nonlinearities result in an extended domain of bistability where the stochastic user equilibrium coexists with stable and unstable oscillations. This study explains the influence of initial conditions on the dynamics of transportation networks and may provide guidance for network design and management.

* Corresponding author. Tel.: +1 734 763 2769.

E-mail addresses: xmzhao@bjtu.edu.cn (X. Zhao), orosz@umich.edu (G. Orosz).

http://dx.doi.org/10.1016/j.physd.2014.02.005
0167-2789/

1. Introduction

Traffic assignment models have been widely used for transportation planning and network design. These models assign demands for origin–destination (OD) pairs and generate the flow pattern on the whole road network. A fundamental concept in assignment problems is the user equilibrium proposed by Wardrop [1], which is the Nash equilibrium for transportation networks [2]. At this state, all used routes on the same OD pair have the same travel cost, while the unused ones have equal or higher cost. The concept of user equilibrium has been extended to deal with a more realistic driver behavior by incorporating uncertainty, leading to the so-called stochastic user equilibrium [3]. This can be viewed as an optimal state for transportation networks and many papers discussed its existence and uniqueness. However, traffic systems that are based on dynamic route adjustment do not necessarily converge to the equilibrium, even when it is proven to exist. Therefore, stability and bifurcation analysis, which addresses whether and how the flow evolves in time, is essential for understanding the traffic behavior.

Day-to-day traffic assignment models are suitable for analyzing the time evolution of the traffic flow on networks, due to their flexibility of accommodating a wide range of behavior rules, levels of aggregation, and traffic models. These models describe how the flow and the related cost (e.g., travel time) change on the network from one day to another. Day-to-day dynamics have attracted significant attention since the seminal work of Horowitz [4], where a two-route scenario was considered and the stability of the equilibrium was explored. In general, day-to-day dynamics can be formulated as deterministic processes or as stochastic processes [5]. In the deterministic framework, it is assumed that travel cost can be perceived perfectly [6–8]. In particular, Smith [6] assumed that the route switch rate is proportional to the difference of travel cost on the routes, while Friesz et al. [7] proposed a day-to-day model that captures both the dynamics of route flows and OD demands. Zhang and Nagurney [8] used a minimum norm projection operator to model the adjustment of day-to-day route flows. All of these papers considered continuous time. However, Watling and Hazelton [9] pointed out that the continuous-time approach had two limitations: (i) continuous-time trip adjustment is not plausible in reality, and (ii) homogeneous population assumptions require additional dispersion modules.

In discrete-time day-to-day models, travelers' route choice is updated daily, in accordance with daily changes in traffic flow, and it is assumed that each trip is executed at most once a day. Specifically, Nagurney and Zhang [10] discretized their continuous model and applied Euler's method to solve the obtained discrete-time dynamical system. He and Liu [11] proposed a "prediction–correction" framework for modeling discrete-time deterministic day-to-day traffic evolution and also gave sufficient conditions for global stability of the equilibrium. They also calibrated their model for a real network with an unexpected disruption. Bie and Lo [12] investigated the stability of user equilibrium pursued by a day-to-day adjustment process and provided tools to determine the stability of the equilibrium and to estimate its domain of attraction. Stochasticity has also been introduced into day-to-day assignment processes, including models formulated as Markov processes [13,14], and models assuming that route choice probabilities depend on the experienced travel times [4,15–17]. In the latter case, the obtained nonlinear dynamical systems are in fact deterministic, since the route choice probabilities are considered to be deterministic functions of averaged quantities.

Travelers forecast their travel costs on different routes by mixing their own experience with information from other sources (e.g., their friends' experience, broadcast, traffic information center etc.), and they make routing decisions according to their inertia and forecasted cost. A common assumption in day-to-day studies is that travelers make the same trip daily. However, in realistic traffic scenarios, many commuters go to one place on some days and to another place on others, so they execute a particular trip in every few days (instead of every day). Recent research provides evidence for the non-daily trips of travelers. By analyzing data collected about multiple days of travel, one can observe variability in travel behavior because people's needs and desires vary significantly in time [18]. By analyzing 149 individuals, Hanson and Huff [19–22] and Raux et al. [23] pointed out that a one-day pattern is not representative of a person's route of travel. Stopher and Zhang [24] classified all trips into twelve tour types, and concluded that a particular tour happens typically two or three times a week, which means that drivers make decision based information that is 2–3 days old. In addition, some traffic policies may bring such delays into the decision making for the entire driving population: in urban areas they often apply restrictions based on parity of the license plate number which forces drivers to make their trips on every other day.

These findings suggest that travelers' experiences are a couple of days old when they choose a route which introduces time delays into the system. Such *driver experience delays* play a key role in determining the arising traffic patterns. As day-to-day models are constructed at the population level, all parameters in this setup, including the delay, represent population averages, that is, heterogeneities in driver behavior are omitted. However, even after taking the population average the system parameters may still vary in time stochastically. The deterministic models considered in this paper describe the mean dynamics of these processes with time-independent parameters. Our goal is to understand how self-excited oscillations of different periods may arise in these systems without external periodic forcing (i.e., without incorporating demand fluctuations). To explore such behavior we vary the system parameters, including the delay, and detect when qualitative changes occur in the dynamics. Such ideas have been coined by Horowitz [4] and Cascetta and Cantarella [25], but no formal analysis has been carried out to understand the effects of the delay on the linear and nonlinear dynamics.

In this paper, for the first time, we utilize state-of-the-art analytical and numerical techniques from dynamical systems theory to investigate the linear and nonlinear stability of the equilibrium when varying delays and other system parameters. This extends the results by Cantarella and Veloná [26] and Cantarella [17] obtained for the linear behavior of non-delayed models. Our generalized model reveals physical phenomena that have not yet been explained before. We show that, apart from extending the linearly unstable domain, the delay also increases the period of arising oscillations significantly so that it can become much larger than the delay itself. Moreover, applying normal form calculations and numerical continuation, we determine regions of bistability in parameter space where the equilibrium coexists with stable and unstable oscillations. In order to quantify the effects of initial conditions we estimate the domain of attraction of the equilibrium by calculating the amplitude of the unstable oscillations. Finally, we remark that larger the delay is the more complex the nonlinear dynamics may become as the number of coexisting oscillations also increases with the delay.

Prior work on vehicular platoons show that time delays can significantly influence the dynamics of transportation systems and change the arising large-scale patterns [27–30]. In platooning problems, delays occur due to driver reaction time that is typically in order of seconds and can significantly affect the nonlinear oscillations with periods in the order of minutes. In day-to-day traffic models, driver experience delays are in the order of 1–3 days and the corresponding nonlinear oscillations have periods of the order of 5–7 days. Nevertheless, the qualitative dynamics are

remarkably similar as both systems exhibit delay-induced bistable behavior.

The remainder of this paper is organized as follows. In Section 2 nonlinear models with driver experience delay are formulated. The linear stability properties of the equilibrium are studied in Section 3, while the effects of nonlinearities are discussed in Section 4. In Section 5 a two-route network is presented and its linear and nonlinear behaviors are analyzed for different delay values. Finally, Section 6 summarizes our findings and suggests future research directions.

2. Nonlinear discrete-time models with driver experience delay

As mentioned above, the dynamics of the flow on transportation networks can be studied using nonlinear discrete-time traffic assignment models that are formulated as deterministic dynamical systems. These models provide effective tools to analyze dynamic day-to-day assignment scenarios and are widely used for transportation design and evaluation. Nonlinearities arise in the route-choice probability function as well as in the cost function and time delays occur because drivers choose the route by averaging their past experiences. In this section we give a description of the modeling framework used in the paper that extends the framework in [15,26] by incorporating the driver experience delay.

In this paper we use the following notation:

N—node set,
A—arc set,
n_A—number of arcs,
W—set of origin–destination (OD) pairs,
K_w—set of routes connecting the OD pair $w \in W$,
n_w—number of routes connecting the OD pair $w \in W$,
d_w—flow demand for the OD pair $w \in W$,
$\Delta_w \in \mathbb{R}^{n_A \times n_w}$—arc-route incident matrix for the OD pair $w \in W$ with entries $\delta_{ak,w} = 1$ if arc $a \in A$ belongs to the route $k \in K_w$ and $\delta_{ak,w} = 0$ otherwise,
$\mathbf{c}_t \in \mathbb{R}^{n_A}$—vector of forecasted arc costs at day t with entries $c_{a,t}$, $a \in A$,
$\mathbf{f}_t \in \mathbb{R}^{n_A}$—vector of arc flows at day t with entries $f_{a,t}$, $a \in A$,
σ, τ—driver experience delays,
$C(\cdot)$—arc cost function,
$F(\cdot)$—network loading function.

We also assume that there is at least one route connecting any OD pair and there are no loops. Fig. B.1 gives an example to explain the notations. In this network, there are four nodes in the node set $N = \{O_1,\ D_1,\ O_2,\ D_2\}$ and five arcs in the arc set $A = \{1,\ 2,\ 3,\ 4,\ 5\}$, that is, $n_A = 5$. The network has two OD pairs $W = \{O_1D_1,\ O_2D_2\}$. The origin–destination pair O_1D_1 has three routes $K_1 = \{1-2,\ 3-4,\ 1-5-4\}$, i.e., $n_1 = 3$; while O_2D_2 has only one route $K_2 = \{5\}$, that is, $n_2 = 1$. Finally, the arc-route incident matrices are given by

$$\Delta_1 = \begin{bmatrix} 1 & 0 & 1 \\ 1 & 0 & 0 \\ 0 & 1 & 0 \\ 0 & 1 & 1 \\ 0 & 0 & 1 \end{bmatrix} \quad \text{and} \quad \Delta_2 = \begin{bmatrix} 0 \\ 0 \\ 0 \\ 0 \\ 1 \end{bmatrix}, \tag{1}$$

for O_1D_1 and O_2D_2, respectively, and they describe the network structure by establishing connections between the arcs and the routes.

Day-to-day assignment models describe the user cost updating and route choice updating processes; that is, how users forecast travel conditions according to their own experience and information from other sources, and how they make their route decisions, either by repeating their previous choice or re-routing according to their forecast. To update these quantities (at the population level) we propose the dynamic model

$$\begin{aligned} \mathbf{c}_{t+1} &= \alpha \sum_{\sigma=0}^{\tau} w_\sigma C(\mathbf{f}_{t-\sigma}) + (1-\alpha)\,\mathbf{c}_t, \\ \mathbf{f}_{t+1} &= \beta\, F(\mathbf{c}_{t+1}) + (1-\beta)\,\mathbf{f}_t. \end{aligned} \tag{2}$$

The first equation describes the cost updating process, that is, how users forecast the costs by combining their delayed experience with those from other sources. Here, w_σ weights travelers experience $\sigma+1$ days ago, that is, drivers predict the cost based on their experiences in the last $\tau+1$ days using the arc cost function $C(\mathbf{f})$. We require that $\sum_{\sigma=0}^{\tau} w_\sigma = 1$. The parameter α is the weight attributed to the forecasted costs against yesterday's actual costs. The second equation updates the flow according to how many users decide to re-route based on the network loading function $F(\mathbf{c})$ and how many are inertial. The parameter β is the weight attributed to reconsidering the previous choice. Notice that the delays are also incorporated in the flow updating process because the function F depends on the "current cost" (forecasted by the drivers to the day the flow is calculated for).

We remark that the parameters α and β are averaged over the population as well as in time. It is difficult to determine the exact value of these parameters but we require $\alpha, \beta \in [0, 1]$ to obtain a physically meaningful model. Similarly, the distributed delay on the right hand side arises after taking averages so that (2) describes the mean dynamics, as is was proven in [31]. Since the individual weights $w_\sigma, \sigma = 0, \ldots, \tau$ are difficult to determine from data, in this paper we consider the simplified setup

$$w_\sigma = \begin{cases} 0 & \text{if } \sigma = 0, \ldots, \tau-1, \\ 1 & \text{if } \sigma = \tau, \end{cases} \tag{3}$$

and vary the parameter τ to investigate the delay-initiated effects. In this case (2) simplifies to

$$\begin{aligned} \mathbf{c}_{t+1} &= \alpha\, C(\mathbf{f}_{t-\tau}) + (1-\alpha)\,\mathbf{c}_t, \\ \mathbf{f}_{t+1} &= \beta\, F(\mathbf{c}_{t+1}) + (1-\beta)\,\mathbf{f}_t, \end{aligned} \tag{4}$$

and from now on we refer the parameter $\tau = 0, 1, 2, \ldots$ as the *driver experience delay*. For $\tau = 0$ Eqs. (2) and (4) recover the non-delayed model in [15,26]. To explore the qualitative changes in the dynamics we will vary the parameters α, β, τ.

In Eq. (4), there are two important nonlinear functions, the *arc cost function* $C(\mathbf{f})$ and the *network loading function* $F(\mathbf{c})$. The arc cost function describes how the arc cost depends on the arc flow. We assume that $C(\mathbf{f})$ is continuously differentiable and strictly monotonously increasing, that is, the Jacobian matrix $\mathbf{Jac}[C(\mathbf{f})]$ is positive definite. One simple example of an arc cost is given by the Bureau of Public Roads (BPR) function

$$C_i(f_1, \ldots, f_{n_A}) = l_0\left(1 + l_1\left(\frac{f_i}{f_c}\right)^4\right), \tag{5}$$

for $i = 1, \ldots, n_A$, where l_0 is the zero-flow cost, l_1 is a dimensionless constant, and f_c is the arc capacity; see the middle panel in Fig. B.3. This function has been calibrated with empirical data and it is widely used in the traffic assignment literature [32–34]. Notice that there is no link interaction in this example, that is, the cost along each arc only depends on the flow on that particular arc, which results in a diagonal Jacobian $\mathbf{Jac}[C(\mathbf{f})]$. The analytical framework presented in this paper can accommodate cost functions with link interactions but we present the numerical results using the BPR function for the sake of simplicity.

The network loading function establishes relations between the arc costs and the arc flows and describes how the demands d_w for

the OD pairs $w \in W$ are assigned on the arcs $a \in A$. For each OD pair, the arc-route relation and flow-demand constraint can be described using the arc-route incidence matrix, that is, $\mathbf{g}_w = \Delta_w^{\mathrm{T}} \mathbf{c}$ and $\mathbf{f} = \Delta_w \mathbf{h}_w$, where $\mathbf{g}_w \in \mathbb{R}^{n_w}$ is the route cost vector and $\mathbf{h}_w \in \mathbb{R}^{n_w}$ is the route flow vector. The route flow $\mathbf{h}_w = d_w \mathbf{p}_w$ contains the route choice probability vector $\mathbf{p}_w = P(\mathbf{g}_w)$. Using these definitions, the network loading function can be constructed as

$$\begin{aligned} F(\mathbf{c}) &= \Sigma_{w\in W} \Delta_w \mathbf{h}_w \\ &= \Sigma_{w\in W} d_w \Delta_w \mathbf{p}_w \\ &= \Sigma_{w\in W} d_w \Delta_w P(\mathbf{g}_w) \\ &= \Sigma_{w\in W} d_w \Delta_w P(\Delta_w^{\mathrm{T}} \mathbf{c}). \end{aligned} \tag{6}$$

We remark that this function satisfies all flow constraints implied by the network structure as these are incorporated in the arc-route incidence matrices Δ_w, $w \in W$.

We assume that the nonlinear route choice probability function $P(\mathbf{g}_w)$ is continuously differentiable and monotonously decreasing thus $F(\mathbf{c})$ has the same properties. Consequently, the Jacobian matrix $\mathbf{Jac}[F(\mathbf{c})] = \Sigma_{w\in W} d_w \Delta_w \mathbf{Jac}[P(\Delta_w^{\mathrm{T}} \mathbf{c})] \Delta_w^{\mathrm{T}}$ is negative semi-definite. A particular example for route choice probability is the logit function

$$P_i(g_{w,1}, \ldots, g_{w,n_w}) = \frac{\exp(-g_{w,i}/\theta)}{\sum_{j=1}^{n_w} \exp(-g_{w,j}/\theta)}, \tag{7}$$

that is often used to represent multiple choice probabilities. Here θ represents the agility of drivers' decision making: the smaller θ is, the smaller price difference is needed to switch the route; see the right panel of Fig. B.3 for a single OD pair with two routes ($n_w = 2$) given by two arcs ($n_A = 2$) implying $g_{w,i} = c_i$, $i = 1, 2$. Arrows indicate the distance between the inflection points.

3. Fixed point and linear stability

In this section, we analyze the dynamics in the vicinity of the stochastic user equilibrium, that is, in a small neighborhood of the fixed point of the deterministic dynamical systems (2), (4). The fixed point is a state that is mapped to itself by the dynamics, that is, $\mathbf{c}_{t+1} = \mathbf{c}_t \equiv \mathbf{c}^*$ and $\mathbf{f}_{t+1} = \mathbf{f}_t \equiv \mathbf{f}^*$ for all t. Substituting this into (2), (4) we obtain

$$\begin{aligned} \mathbf{c}^* &= C(\mathbf{f}^*), \\ \mathbf{f}^* &= F(\mathbf{c}^*), \end{aligned} \tag{8}$$

which allows us to derive the equilibrium cost $\mathbf{c}^*$ and the equilibrium flow $\mathbf{f}^*$. Notice that the equilibrium is independent of the delay. Since the continuously differentiable functions $C(\mathbf{f})$ and $F(\mathbf{c})$ are strictly monotonously increasing and monotonously decreasing, respectively, the uniqueness of the equilibrium can be guaranteed [2,35]. Now we derive necessary and sufficient conditions which guarantee that system (4) converges to the fixed point (8) when started from a small neighborhood, i.e., this state is linearly asymptotically stable [36,37]. In order to obtain such conditions we linearize the system about the equilibrium and calculate the eigenvalues of the corresponding Jacobian matrix evaluated at the fixed point. If all eigenvalues are located inside the unit circle in the complex plane then the fixed point is linearly asymptotically stable [36,37].

First, we rewrite (4) as a dynamical system that maps the state at time t to the state at time $t+1$. Thus, we introduce $(2+\tau) \times n_A$ state variables:

$$\left.\begin{aligned} \mathbf{y}_{1,t} &= \mathbf{c}_t \\ \mathbf{y}_{2,t} &= \mathbf{f}_t \end{aligned}\right\} 2 \times n_A \text{ variables}$$
$$\left.\begin{aligned} \mathbf{y}_{3,t} &= \mathbf{f}_{t-1} \\ \mathbf{y}_{4,t} &= \mathbf{f}_{t-2} \\ &\vdots \\ \mathbf{y}_{\tau+1,t} &= \mathbf{f}_{t-\tau+1} \\ \mathbf{y}_{\tau+2,t} &= \mathbf{f}_{t-\tau} \end{aligned}\right\} \tau \times n_A \text{ variables} \tag{9}$$

which allow us to reformulate (4) as

$$\begin{aligned} \mathbf{y}_{1,t+1} &= \alpha\, C(\mathbf{y}_{\tau+2,t}) + (1-\alpha)\, \mathbf{y}_{1,t} \\ \mathbf{y}_{2,t+1} &= \beta\, F\Big[\alpha \cdot C(\mathbf{y}_{\tau+2,t}) + (1-\alpha)\, \mathbf{y}_{1,t}\Big] + (1-\beta)\, \mathbf{y}_{2,t} \\ \mathbf{y}_{3,t+1} &= \mathbf{y}_{2,t} \\ \mathbf{y}_{4,t+1} &= \mathbf{y}_{3,t} \\ &\vdots \\ \mathbf{y}_{\tau+1,t+1} &= \mathbf{y}_{\tau,t} \\ \mathbf{y}_{\tau+2,t+1} &= \mathbf{y}_{\tau+1,t}. \end{aligned} \tag{10}$$

By defining the $(2+\tau) \times n_A$-dimensional state vector $\hat{\mathbf{y}}_t = \mathrm{col}[\mathbf{y}_{1,t}, \mathbf{y}_{2,t}, \ldots, \mathbf{y}_{\tau+2,t}]$ one may formally write

$$\hat{\mathbf{y}}_{t+1} = \hat{H}(\hat{\mathbf{y}}_t). \tag{11}$$

The fixed point of this dynamical system can be written as $\hat{\mathbf{y}}^* = \mathrm{col}[\mathbf{c}^*, \mathbf{f}^*, \ldots, \mathbf{f}^*]$ which indeed satisfies $\hat{\mathbf{y}}^* = \hat{H}(\hat{\mathbf{y}}^*)$. Introducing the perturbation $\hat{\mathbf{x}}_t = \hat{\mathbf{y}}_t - \hat{\mathbf{y}}^*$, the linearized equation can be written as

$$\hat{\mathbf{x}}_{t+1} = \hat{\mathbf{J}}\, \hat{\mathbf{x}}_t, \tag{12}$$

where

$$\hat{\mathbf{J}} = \begin{bmatrix} (1-\alpha)\mathbf{I} & 0 & 0 & 0 & \cdots & 0 & \alpha \mathbf{J}_C \\ (1-\alpha)\beta \mathbf{J}_F & (1-\beta)\mathbf{I} & 0 & 0 & \cdots & 0 & \alpha\beta \mathbf{J}_F \mathbf{J}_C \\ 0 & \mathbf{I} & 0 & 0 & \cdots & 0 & 0 \\ 0 & 0 & \mathbf{I} & 0 & \cdots & 0 & 0 \\ \vdots & \vdots & 0 & \mathbf{I} & \ddots & 0 & 0 \\ \vdots & \vdots & \vdots & \ddots & \ddots & \ddots & \vdots \\ 0 & 0 & 0 & 0 & \cdots & \mathbf{I} & 0 \end{bmatrix}. \tag{13}$$

Here, we used the notation $\mathbf{J}_C = \mathbf{Jac}[C(\mathbf{f}^*)]$ and $\mathbf{J}_F = \mathbf{Jac}[F(\mathbf{c}^*)]$ while $\mathbf{I}$ denotes the n_A-dimensional identity matrix. Indeed, the $(2+\tau)n_A$-dimensional Jacobian matrix $\hat{\mathbf{J}} = \mathbf{Jac}[\hat{H}(\hat{\mathbf{y}}^*)]$ is evaluated at the fixed point and all of its eigenvalues must be inside the unit circle in the complex plane to ensure the stability of (8).

Theorem 1. *The $(2+\tau)n_A$ eigenvalues of $\hat{\mathbf{J}}$ are given by*

$$\det\big[(\lambda+\alpha-1)(\lambda+\beta-1)\lambda^{\tau}\mathbf{I} - \alpha\beta\lambda \mathbf{J}_F \mathbf{J}_C\big] = 0. \tag{14}$$

Furthermore, when the matrix $\mathbf{J}_F\mathbf{J}_C$ is diagonalizable Eq. (14) can be rewritten as

$$(\lambda+\alpha-1)(\lambda+\beta-1)\lambda^{\tau} - \alpha\beta\lambda\gamma_i = 0, \tag{15}$$

for $i = 1, \ldots, n_A$, where γ_i is the ith eigenvalue of the matrix $\mathbf{J}_F\mathbf{J}_C$.

The proof of this theorem is provided in Appendix A.

Corollary 1. *For $\tau = 0$, the $2n_A$ eigenvalues can be obtained from*

$$\det\big[(\lambda+\alpha-1)(\lambda+\beta-1)\mathbf{I} - \alpha\beta \mathbf{J}_F \mathbf{J}_C\big] = 0, \tag{16}$$

and for diagonalizable $\mathbf{J}_F\mathbf{J}_C$ we have

$$(\lambda+\alpha-1)(\lambda+\beta-1) - \alpha\beta\gamma_i = 0, \tag{17}$$

for $i = 1, \ldots, n_A$. This corresponds to the results in [17,26].

Corollary 2. *For $\tau > 0$ there are always n_A zero eigenvalues, and other $(1+\tau)n_A$ eigenvalues are given by*

$$\det\left[(\lambda+\alpha-1)(\lambda+\beta-1)\lambda^{\tau-1}\mathbf{I}-\alpha\beta\mathbf{J}_F\mathbf{J}_C\right]=0, \tag{18}$$

and for diagonalizable $\mathbf{J}_F\mathbf{J}_C$ we have

$$(\lambda+\alpha-1)(\lambda+\beta-1)\lambda^{\tau-1}-\alpha\beta\gamma_i=0, \tag{19}$$

for $i=1,\ldots,n_A$.

As mentioned above in order to ensure the linear stability of the fixed point all the $(2+\tau)n_A$ eigenvalues must be inside the unit circle in the complex plane. The goal of stability analysis is to determine the parameter domains where stability is maintained without explicitly calculating the eigenvalues. The stability of the fixed point changes when eigenvalues cross the unit circle while varying parameters. Three qualitatively different stability losses are possible [17,26,36,37]:

1. A real eigenvalue crosses the unit circle at 1 (called fold bifurcation) which can result in additional fixed points;
2. A real eigenvalue crosses the unit circle at -1 (called flip or period-doubling bifurcation) which leads to oscillations of period 2 (days);
3. A pair of complex conjugate eigenvalues crosses the unit circle (called Neimark–Sacker bifurcation) which results in oscillations of period $2\pi/\phi > 2$ (days), where $\phi \in (0,\pi)$ is the angle of the crossing eigenvalue with positive imaginary part.

These conditions can be tested by inserting $\lambda = 1, \lambda = -1$, and $\lambda = \exp(\mathrm{i}\phi)$ into (14) or (15) and the corresponding curves can be plotted on a chosen parameter plane. We found that in the physically relevant domain $\alpha, \beta \in (0,1)$ the system may lose stability via flip and Neimark–Sacker bifurcations which corresponds to the uniqueness of the equilibrium. Using (14), (15) stability charts will be drawn for the example in Section 5 to demonstrate graphically how the stability of the fixed point is influenced by the delay.

4. Bifurcations and domains of attraction

The linear stability analysis of the fixed point gives a boundary separating the linearly stable region and the unstable region in parameter space. When parameters are chosen from the stable region the linearized system (12), (13) converges to the fixed point (8) independent of the choice of initial conditions. This suggests that the domain of attraction is the whole state space. However, this may not be true for the corresponding nonlinear system where linear stability only ensures convergence in a small neighborhood of the fixed point. Here, by definition, the domain of attraction of the fixed point is the set of initial conditions for which trajectories converge to the fixed point. This may be estimated by running a large number of simulations. However, considering the $(2+\tau)n_A$-dimensional state space, this may not be feasible for systems of realistic size.

In this paper, instead of running extensive simulations, we take a systematic approach to estimate the domain of attraction. Based on the theory of dynamical systems the essential nonlinear dynamics of the system can be captured by the low dimensional dynamics occurring on invariant manifolds embedded in the $(2+\tau)n_A$-dimensional state space. These manifolds are 1-dimensional for flip and 2-dimensional for Neimark–Sacker bifurcations. Choosing the parameters close to the stability boundary and approximating the nonlinearities by Taylor expansion up to cubic order, one may use a sequence of nonlinear coordinate transformations and derive the low-dimensional normal form equations that govern the dynamics on the invariant manifold. This way the amplitude, period, and stability of the arising oscillations can be determined; see Appendix B for more details. Transforming the equations back to the original physical coordinates allow one to characterize the dynamics of the system.

In particular, for flip bifurcation the normal form calculations result in the invariant motion

$$\begin{bmatrix}\mathbf{c}_t\\ \mathbf{f}_t\end{bmatrix}=\begin{bmatrix}\mathbf{a}_c(\beta)\\ \mathbf{a}_f(\beta)\end{bmatrix}(-1)^t+\begin{bmatrix}\mathbf{c}^*\\ \mathbf{f}^*\end{bmatrix}, \tag{20}$$

that has period $T_F = 2$ (days) and the amplitudes of oscillations are given by $\mathbf{a}_c, \mathbf{a}_f \in \mathbb{R}^{n_A}$. These depend on the bifurcation parameter, which is chosen to be β in this case, so that they are proportional to $\sqrt{\beta-\beta_{\mathrm{cr}}}$ where the critical value β_{cr} gives the stability boundary. Similarly, for Neimark–Sacker bifurcation we obtain

$$\begin{bmatrix}\mathbf{c}_t\\ \mathbf{f}_t\end{bmatrix}=\begin{bmatrix}\mathbf{b}_c(\beta)\\ \mathbf{b}_f(\beta)\end{bmatrix}\cos(\phi\, t+\vartheta)+\begin{bmatrix}\mathbf{c}^*\\ \mathbf{f}^*\end{bmatrix}, \tag{21}$$

where the amplitudes $\mathbf{b}_c, \mathbf{b}_f \in \mathbb{R}^{n_A}$ are also proportional to $\sqrt{\beta-\beta_{\mathrm{cr}}}$. The period $T_{\mathrm{NS}} = 2\pi/\phi$ (days) is given by the angle of the crossing eigenvalue $\phi \in (0,\pi)$ at the critical point $\beta = \beta_{\mathrm{cr}}$. As the motion is invariant the phase angle ϑ is arbitrary.

As mentioned above, the normal form calculations also reveal the stability of the arising nonlinear oscillations. Two different cases are possible. For *supercritical bifurcation*, stable oscillations appear in the parameter region where the fixed point is unstable as shown in the left panel of Fig. B.2 where the minimum and maximum of oscillations are plotted together with the fixed point (horizontal line). Stable and unstable states are represented by solid and dashed curves and this notation is used consistently in the remaining part of this paper. In this case linear stability of the fixed point indicates global stability and the corresponding domain of attractions is the whole state space. On the other hand, for *subcritical bifurcation*, unstable oscillations occur in the parameter region where the fixed point is linearly stable; see the right panel of Fig. B.2. This means that for initial conditions chosen close to the fixed point the system converges to the fixed point, but this is not the case for all initial conditions. The arising unstable oscillations, while rarely visible in practice, are significant as they give the "threshold" for how large perturbations are allowed so that the system still approaches the fixed point. More precisely, the stable manifold of the unstable periodic orbit gives the boundary of the domain of attractions in state space. The figure suggests that this domain increases as the parameter moves away from the critical point. Appendix B provides some details about how the criticality of the flip and Neimark–Sacker bifurcations are derived and show their applicability using the example in Section 5. Similar calculations have also been recently carried out by Habib et al. in [38].

Indeed, both (20) and (21) are approximations and only describe the oscillations in the vicinity of the bifurcation point. To analyze the invariant motions of the fully nonlinear system (10), (11) one needs to use numerical techniques. Numerical simulations allow one to study stable motion as the system converges to stable states (for a subset of initial conditions). However, this becomes very difficult when one wishes to compute unstable states, especially unstable oscillations. A different approach, called numerical continuation, may be taken by formulating periodic orbits as boundary value problems and using Newton iterations to correct the initial guess. Then the computed orbit can be used to initialize the Newton iterations when changing the bifurcation parameter. This allows one to reproduce bifurcation diagrams like those in Fig. B.2 and to repeat this for the fully nonlinear system; see already Figs. B.7 and B.9. Notice that the global picture reveals what happens in the subcritical case for initial conditions that do not converge to the fixed point: the system converges to large amplitude oscillations that arise when the oscillatory

branch folds back. This creates regions of bistability where despite having a stable fixed point one can observe sustained oscillations for a subset of initial conditions. To compute invariant period-2 branches arising from the flip bifurcation point we use the software MATCONT [39]. In fact, this is analogous to computing the fixed point of the double map $\hat{H}\big(\hat{H}(\hat{\mathbf{y}})\big)$; cf. (11). To compute the branches arising from the Neimark–Sacker bifurcation point one needs to compute invariant tori in state space. In order to do this we adapted the method developed by Dankowicz and Thakur [40] for discrete time systems.

5. Two-route example

To illustrate the linear and nonlinear phenomena described above, we consider a simple network as shown on the left panel of Fig. B.3 with one origin–destination pair and two routes given by two arcs. The arc cost function for this system is given by Eq. (5), that is,

$$C(\mathbf{f}) = \begin{bmatrix} C_1(f_1, f_2) \\ C_2(f_1, f_2) \end{bmatrix} = \begin{bmatrix} l_0 \left(1 + l_1 \left(\frac{f_1}{f_c}\right)^4\right) \\ l_0 \left(1 + l_1 \left(\frac{f_2}{f_c}\right)^4\right) \end{bmatrix}, \tag{22}$$

which is plotted in the middle panel of Fig. B.3, where the zero-flow cost l_0, the cost range $l_0 l_1$, and the arc capacity f_c are shown. Since there is only one OD pair in the network the w index can be omitted when constructing the network loading function (6). Moreover, the arcs and the routes in the system are identical implying that the arc-route incident matrix Δ is the 2×2 identity matrix. Using the route choice probability function (7), the network loading function can be written as

$$F(\mathbf{c}) = \begin{bmatrix} F_1(c_1, c_2) \\ F_2(c_1, c_2) \end{bmatrix} = \begin{bmatrix} \dfrac{d}{1 + \exp\big(-(c_2 - c_1)/\theta\big)} \\ \dfrac{d}{1 + \exp\big(-(c_1 - c_2)/\theta\big)} \end{bmatrix}. \tag{23}$$

This is depicted on the right panel of Fig. B.3 where the demand d and the distance between the two inflection points are shown. As can be seen, the parameter θ gives the characteristic price difference needed to switch the route.

5.1. Linear stability

One may show that the fixed point of the two route system is given by

$$\begin{aligned} f_1^* &= f_2^* = d/2, \\ c_1^* &= c_2^* = l_0\left(1 + l_1\left(\frac{d}{2f_c}\right)^4\right), \end{aligned} \tag{24}$$

which is unique due to the monotonous properties of functions (22), (23). By evaluating the Jacobian for the arc cost function (22) and the network loading function (23) at the fixed point (24), we obtain

$$\left.\begin{aligned} \mathbf{J}_C &= \frac{l_0 l_1 d^3}{2f_c^4} \begin{bmatrix} 1 & 0 \\ 0 & 1 \end{bmatrix} \\ \mathbf{J}_F &= \frac{d}{4\theta} \begin{bmatrix} -1 & 1 \\ 1 & -1 \end{bmatrix} \end{aligned}\right\} \Rightarrow \mathbf{J}_F\mathbf{J}_C = q \begin{bmatrix} -1 & 1 \\ 1 & -1 \end{bmatrix}, \tag{25}$$

where the dimensionless parameter

$$q = \frac{l_0 l_1 d^4}{8\theta f_c^4} \geq 0 \tag{26}$$

contains the "width" and the "height" of the dynamical regimes of the nonlinear functions (22), (23). Here the matrix $\mathbf{J}_F\mathbf{J}_C$ (25) can be diagonalized and has the two eigenvalues $\gamma_1 = 0$ and $\gamma_2 = -2q \leq 0$, that is, Eq. (15) leads to the equations

$$(\lambda + \alpha - 1)(\lambda + \beta - 1)\lambda^\tau = 0, \tag{27}$$

$$(\lambda + \alpha - 1)(\lambda + \beta - 1)\lambda^\tau + \alpha\beta\lambda 2q = 0. \tag{28}$$

The eigenvalues given by (27) are located inside the unit circle in the complex plane if and only if

$$0 < \alpha < 2 \quad \text{and} \quad 0 < \beta < 2. \tag{29}$$

At $\alpha = 0$ and $\beta = 0$ a real eigenvalue crosses the unit circle at 1 (fold bifurcation occurs), while at $\alpha = 2$ and $\beta = 2$ a real eigenvalue crosses the unit circle at -1 (flip bifurcation occurs). Recall that the physically realistic parameter domain is given by $0 < \alpha < 1$ and $0 < \beta < 1$.

For $q = 0$ Eq. (28) is equivalent to (27) while the $q > 0$ case requires further analysis. By substituting $\lambda = 1$ into (28) one can show that the fold stability boundaries are still at $\alpha = 0$ and $\beta = 0$, while substituting $\lambda = -1$ gives the flip stability boundaries

$$\begin{aligned} \beta &= \frac{4 - 2\alpha}{2 - \alpha(1 - 2q)}, \quad \text{if } \tau = 0, 2, 4, \ldots \\ \beta &= \frac{4 - 2\alpha}{2 - \alpha(1 + 2q)}, \quad \text{if } \tau = 1, 3, 5, \ldots. \end{aligned} \tag{30}$$

Finally, substituting $\lambda = \exp(\mathrm{i}\phi)$, $\phi \in (0, \pi)$, separating the real and the imaginary parts, and using some algebraic manipulations one can show that a pair of complex conjugate eigenvalues crosses the unit circle at the Neimark–Sacker curve given by

$$\begin{aligned} \alpha\beta &= \frac{2(1 - \cos\phi)\sin\phi}{\sin\phi + \Big[\sin(\tau\phi) - \sin\big((\tau - 1)\phi\big)\Big]2q}, \\ \alpha + \beta &= \frac{2(1 - \cos\phi)\big(\sin\phi + \sin(\tau\phi)2q\big)}{\sin\phi + \Big[\sin(\tau\phi) - \sin\big((\tau - 1)\phi\big)\Big]2q}. \end{aligned} \tag{31}$$

From these equations α and β can be calculated as a function $\phi \in (0, \pi)$ and the corresponding parametric curves can be plotted on the (α, β)-plane. All curves generated by (29), (30), (31) are plotted in Fig. B.4 for different values of τ and q where the shaded domain corresponds to linear stability of the fixed point and the physically relevant domain is bounded by dashed lines. Comparing the different panels one can observe that the size of the stable domain is reduced when q and τ are increased. In the physically relevant domain instabilities only occur for $q > 1/2$. The flip boundaries $\alpha = 2$, $\beta = 2$, and (30) are shown as black curves and these are indeed the same in every second row. The Neimark–Sacker boundaries (31) are shown as red curves and the maximum number of Neimark–Sacker curves increases by one for every odd value of the delay.

5.2. Normal form calculations

As explained in Section 4 considering the nonlinearity of the system up to the cubic order, we can transform the model into normal form in the vicinity of the flip bifurcation or the Neimark–Sacker bifurcation. To demonstrate the fundamental nonlinear phenomena we focus on the cases $\tau = 0$ and $\tau = 1$ because only flip bifurcations occur for $\tau = 0$ and only Neimark–Sacker bifurcations occur for $\tau = 1$, as shown in the first two rows of Fig. B.4. Indeed, the methods can also be used for $\tau > 1$ where both types of bifurcations occur making the global picture more intricate with many coexisting solutions. The details of the normal form calculations are shown in Appendix B and here we only state the main results.

For the flip bifurcation ($\tau = 0$) the first equation in (30) gives the critical value

$$\beta_{cr} = \frac{4 - 2\alpha}{2 - \alpha(1 - 2q)}, \tag{32}$$

and the normal form calculations give the flow oscillations

$$f_{1,t} = \sqrt{S_F(\beta - \beta_{cr})}\,(-1)^t + d/2, \tag{33}$$

where

$$S_F = \frac{3d^2(\alpha - 2)\big[2 - \alpha(1 - 2q)\big]^2}{16\alpha q\big[12(1 - \alpha) + \alpha^2(3 - 4q^2)\big]}. \tag{34}$$

As the fixed point looses stability when β is increased the sign of S_F determines the criticality of the bifurcation:

$$\begin{cases} S_F < 0 & \text{if } 0 < \alpha < \dfrac{2\sqrt{3}}{2q + \sqrt{3}} \Rightarrow \text{ subcritical flip,} \\ S_F > 0 & \text{if } \dfrac{2\sqrt{3}}{2q + \sqrt{3}} < \alpha < 2 \Rightarrow \text{ supercritical flip,} \end{cases} \tag{35}$$

which is demonstrated on the left panel of Fig. B.5 for different values of the demand d and $q = 1$. Note that in order to keep q constant we change θ parallel to d while keeping $l_0 = 8, l_1 = 1, f_c = 1$ constant; cf. (26).

For the Neimark–Sacker bifurcation ($\tau = 1$) eliminating ϕ from the formulae (31) the critical value

$$\beta_{cr} = \frac{\alpha}{\alpha(1 + 2q) - 1}, \tag{36}$$

can be obtained. On the other hand, eliminating β from (31) gives the crossing angle

$$\phi = \arccos\left(1 - \frac{\alpha^2(1 + 2q)}{2\big[\alpha(1 + 2q) - 1\big]}\right). \tag{37}$$

The normal form calculations result in

$$f_{1,t} = \sqrt{S_{NS}(\beta - \beta_{cr})}\,\cos(\phi t + \vartheta) + d/2, \tag{38}$$

where

$$S_{NS} = \frac{d^2\big[\alpha(1 + 2q) - 1\big]^2}{2\alpha^2 q\big[2\alpha q(1 + 2q) - 2q - 3\big]}. \tag{39}$$

Again, the sign of S_{NS} determines the criticality of the bifurcation:

$$\begin{cases} S_{NS} < 0 & \text{if } \alpha_0 < \alpha < \dfrac{3 + 2q}{2q(1 + 2q)} \Rightarrow \text{ subcritical NS,} \\ S_{NS} > 0 & \text{if } \alpha > \dfrac{3 + 2q}{2q(1 + 2q)} \Rightarrow \text{ supercritical NS,} \end{cases} \tag{40}$$

where α_0 is the lowest possible value of α along the stability boundary; see the second row of Fig. B.4. For $q > 1/2$ it is given by the location of the vertical asymptote of the Neimark–Sacker curve, i.e., $\alpha_0 = 1/(1 + 2q)$, cf. (36). Eq. (40) is demonstrated on the right panel of Fig. B.5 for different values of the demand d and $q = 1$.

Fig. B.6 summarizes the dynamics for the flip bifurcation ($\tau = 0$) and the Neimark–Sacker bifurcation ($\tau = 1$) when $q = 1$ and $d = 1$. Both subcritical and supercritical bifurcations are found and the change between the two behaviors is marked by a star which corresponds to the conditions (35) and (40). In both cases subcriticality is observed for small values of α that changes into supercriticality as α is increased. In the light gray region the fixed point is globally stable while in the white region it is unstable. The dark gray region is a bistable region, where both the fixed point and the large amplitude oscillations are linearly stable and their domains of attractions are separated by the stable manifold of the unstable oscillation. The boundaries of the bistable domain are given by the linear stability boundary of the fixed point (red curve) and the fold boundary of the oscillatory solutions (blue curve); see already Figs. B.7 and B.9. Notice that for $\tau = 1$ the bistable domain is much larger compared to the $\tau = 0$ case, which indicates that, apart from increasing the domain of linear instability for the fixed point, the delay also increases the bistable domain. To fully explore the global behavior and its dependence on the delay τ and the demand d we use numerical continuation and simulation as explained below.

5.3. Global dynamics

In this section we show the details of the dynamical behavior in the different shaded domains in Fig. B.6. We demonstrate the fundamental differences between the global dynamics implied by super- and subcritical bifurcations and highlight the effects of the delay on nonlinear behavior. In particular, we present the bifurcation diagrams for $\alpha = 1$ where the bifurcations are supercritical for both $\tau = 0$ and $\tau = 1$, and also for $\alpha = 1/2$ where the bifurcations are subcritical. We fix $q = 1$, that is, for the flip bifurcation $\alpha = 1$ implies $\beta_{cr} = 2/3$ and $\alpha = 1/2$ implies $\beta_{cr} = 6/5$; see (32) and the left panel of Fig. B.6. For the Neimark–Sacker bifurcation $\alpha = 1$ implies $\beta_{cr} = 1/2$ and $\alpha = 1/2$ implies $\beta_{cr} = 1$; see (36) and the right panel of Fig. B.6. To demonstrate the global behavior, we also display the invariant orbits in state space and show the time evolution of the flow for chosen sets of parameters.

For $\tau = 0$ flip bifurcations take place and the arising branches represent oscillations of period 2 (days). These states constitute the fixed point of the double map $\hat{H}\big(\hat{H}(\hat{\mathbf{y}})\big)$ (cf. (11)), which can be computed by the numerical continuation package MATCONT [39]. The left and right columns of Fig. B.7 show the branches arising from supercritical and subcritical flip bifurcations, respectively. In each panel, the maximum and the minimum of the flow oscillations are depicted as a function of the bifurcation parameter β. Stable and unstable states are represented by solid and dashed curves and the horizontal line at $d/2$ represents the fixed point. The results of the analytical normal form calculations (33), (34) are shown as black curves while colored curves are obtained by numerical continuation. The analytical and numerical results match very well in the vicinity of the flip bifurcation (black cross at β_{cr}).

In case of the supercritical bifurcation (left column) linear stability of the equilibrium ($\beta < \beta_{cr}$) implies global stability and when the equilibrium is unstable ($\beta > \beta_{cr}$), stable oscillations appear whose amplitude increases with β. For large β, the curves exceed the horizontal lines at 0 and 1 which indicate the physically relevant domain for the flow. (By enforcing explicit flow constraint in the model one may ensure that the flow stays between these lines.) In case of subcritical bifurcation (right column), the unstable branches of oscillations fold back (black star at β_{sub}) and the oscillations become stable. This leads to three domains of qualitatively different dynamics. For $\beta < \beta_{sub}$ the fixed point is globally stable while for $\beta > \beta_{cr}$ the fixed point is unstable and the large-amplitude oscillations are globally stable. For $\beta_{sub} < \beta < \beta_{cr}$ bistability is observed where the stable fixed point and the stable large-amplitude oscillations coexist with unstable oscillations. Depending on the initial conditions the system may approach the fixed point or the large-amplitude oscillations. Their domains of attraction are separated by the stable manifold of the unstable state.

The different rows in Fig. B.7 correspond to different values of the demand d while $q = 1$ is kept fixed. In particular, we chose

$\theta = d^4$ while fixing $l_0 = 8, l_1 = 1, f_c = 1$; cf. (26). One may observe that the fixed point is located at $d/2$ (see (24)) and that the amplitude is also proportional to d (see (33), (34)). The flip bifurcation point (cross at $\beta = \beta_{cr}$) does not move when changing d as q is kept fixed, cf. (32). Moreover, the fold bifurcation point (star at $\beta = \beta_{sub}$) does not move significantly with d. Such invariance is observed for the entire subcritical regime $0 < \alpha < 2\sqrt{3}/(2q+\sqrt{3})$ (cf. (35)) which means that the chart shown in the left panel of Fig. B.6 is approximately the same for all d.

In order to demonstrate the time evolution of the system when it undergoes super- or subcritical flip bifurcation, we marked the points A_1, B_1, C_1, D_1 in the middle panels of Fig. B.7. Fig. B.8 displays the corresponding trajectories in state space (c_1, f_1) on the left and shows the time evolution of the flow f_1 on the right. The initial flow $f_{1,0}$ is chosen as explained below and we use $f_{2,0} = d - f_{1,0}, c_{i,0} = C(f_{i,0}), i = 1, 2$. In the supercritical case, point A_1 is at $\beta = 0.6$ that is in the region where the fixed point is globally stable while B_1 is at $\beta = 0.75$ that is in the region where oscillations are globally stable. In both cases $f_{1,0} = 0.6$ is selected and the simulation results are shown in the corresponding panels of Fig. B.8: for A_1 the system approaches the fixed point while for B_1 it approaches oscillations of period-2 days. (The attractors are marked by blue circles in state space.) In the subcritical case, both points C_1 and D_1 are chosen for the same parameter $\beta = 1.1$ in the bistable region, so they only differ in initial conditions: for point C_1 we choose $f_{1,0} = 0.6319$ while for D_1 we have $f_{1,0} = 0.6320$. The corresponding numerical simulations in Fig. B.8 stay close to the unstable orbit (red triangle) before approaching the stable fixed point or the stable large-amplitude period-2 oscillations (blue circles). This demonstrates the role of the unstable motion in separating the domains of attractions of the stable motions.

For $\tau = 1$ Neimark–Sacker bifurcations occur and the corresponding branches represent oscillations with period close to $2\pi/\phi$ where ϕ is the crossing angle given by (37). Considering $q = 1$ for $\alpha = 1$ and $\alpha = 1/2$ we obtain $\phi = \arccos(1/4) \approx 0.42\pi$ giving the period $2\pi/\phi \approx 4.77$ (days). As this is an irrational number the corresponding periodic motion becomes a torus in state space (where one of the periods is 1 while the other is close to $2\pi/\phi$). To compute tori we adapt the Newton iteration scheme developed in [40] for continuous-time systems. In particular, we modify the interpolation that is used to create a more dense representation of the torus so that, instead of interpolating in time, we interpolate in state space. After calculating the torus for a given parameter β, the result is used to initialize the Newton iterations for nearby β-s. This way the branch of oscillations is computed.

The left and right columns of Fig. B.9 show the branches arising from the supercritical and subcritical Neimark–Sacker bifurcations (crosses at β_{cr}). The notation is the same as in Fig. B.7 and indeed the analytical (black) curves given by (38), (39) match the numerical ones (colored) in the vicinity of the critical point. Note that the amplitude is still proportional to d. Again, in the supercritical case, $\beta < \beta_{cr}$ and $\beta > \beta_{cr}$ correspond to regions where the fixed point and the oscillations are globally stable, respectively. In the subcritical case these regions are given by $\beta < \beta_{sub}$ and $\beta > \beta_{cr}$, while bistability is observed for $\beta_{sub} < \beta < \beta_{cr}$. Changing the demand d still does not change the location of the fold bifurcation (star at $\beta = \beta_{sub}$) significantly, and this holds for all feasible $\alpha_0 < \alpha < (3 + 2q)/(2q(1 + 2q))$; cf. (40). This makes the right panel of Fig. B.6 (approximately) demand-independent.

To observe the main difference caused by the delay we marked the points A_2, B_2, C_2, D_2 in the middle panels of Fig. B.9 and display the corresponding simulation results in Fig. B.10. The orbits are shown in state space (f_1, c_1) (left column) together with the time-profiles of f_1 (right column) and the same notation is used as in Fig. B.8. For the initial conditions of the delayed model, we set $f_{1,-1}$ as explained below while considering $f_{2,-1} = d - f_{1,-1}$, $c_{i,-1} = C(f_{i,-1}),\ i = 1, 2$ and generate the values for $t = 0$ using the non-delayed model. Points A_2 and B_2 are located at $\beta = 0.47$ and $\beta = 0.6$ and we choose $f_{1,-1} = 0.6$. The corresponding simulation results show the globally stable fixed point and globally stable oscillations. Notice that the geometry of the orbit in state spaces and the time profiles (including the period) change significantly compared to the non-delayed case (cf. B_1 in Fig. B.8 with B_2 in Fig. B.10). Points C_2 and D_2 are located at $\beta = 0.85$ in the bistable domain and only differ in initial conditions: choosing $f_{1,-1} = 0.6248$ and $f_{1,-1} = 0.6250$ lead the system to the fixed point and to the large-amplitude oscillations, respectively. Notice that the geometry of the stable and unstable tori are much more complicated than the period-2 orbits (cf. C_1 and D_1 in Fig. B.8 with C_2 and D_2 in Fig. B.10) which lead to more complicated oscillations in the time domain as well.

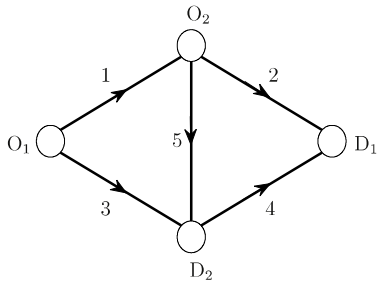

Fig. B.1. A transportation network with four nodes $N = \{O_1, D_1, O_2, D_2\}$ and $n_A = 5$ arcs $A = \{1, 2, 3, 4, 5\}$. Arrows represent the direction of the flow. There are two origin–destination pairs $W = \{O_1D_1, O_2D_2\}$, so that O_1D_1 has $n_1 = 3$ routes: $K_1 = \{1-2, 3-4, 1-5-4\}$, while O_2D_2 has $n_2 = 1$ route: $K_2 = \{5\}$.

6. Conclusion and discussion

Day-to-day traffic dynamics were studied by incorporating driver experience delays that arise due to the fact that many travelers execute their trips in every few days. We proposed a nonlinear, discrete-time, deterministic model that explicitly includes the nonlinear route choice probability function of drivers as well as the driver experience delay. The stochastic user equilibrium is a fixed point of this deterministic dynamical system. We analyzed the dynamics at the linear and the nonlinear level by using stability analysis, normal form calculations, numerical continuation and simulation. The theoretical results were demonstrated on a simple two-link network.

We found that the delay impacts the dynamics significantly as it increases the linearly unstable domain in parameter space. Moreover, we identified regions of bistability where, depending on the initial conditions, the traffic system converges to the equilibrium (with equal costs on used routes) or develops large-amplitude oscillations. We showed that even having 1 day delay in route selection increases the period of the oscillations significantly (from 2 to appr. 5 days in our example). Moreover, the delay makes the bistable behavior much more pronounced by enlarging the corresponding domain in parameter space.

Our study demonstrates that linear design is not adequate for transportation networks but nonlinear phenomena must be taken into account, especially when delays are present. In particular, examining the effects of initial conditions on the dynamics provides an explanation about long period oscillations in transportation networks that may appear and disappear from time to time even without significant changes in the demands. To avoid such phenomena, the designer has two major tools to influence the nonlinear dynamics. One is to design the physical structure of the road network and the corresponding maximal flow f_c, the zero flow cost l_0, and the cost range l_0l_1 appropriately. On

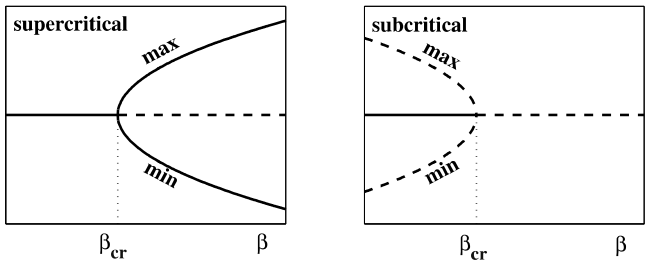

Fig. B.2. Bifurcation diagrams for supercritical and subcritical bifurcations showing the minimum and the maximum of the oscillating states as the function of the bifurcation parameter β. The horizontal line represents the fixed point. Stable states are represented by solid curves while unstable states are represented by dashed curves. Note that the difference between flip and Neimark–Sacker bifurcations appears in the period as $T_F = 2$ and $T_{NS} > 2$ (not visible in this figure).

the other hand, one may tune the driver parameters α, β, θ, d by introducing tolls as well as by providing feedback to the drivers using advanced information systems. The goal is to create systems which stay in the parameter domain with a globally stable equilibrium.

The methodology presented in this paper provides a first insight to the effects of driver experience delay on day-to-day traffic dynamics and the approach can also be used to study the nonlinear dynamics of more complicated transportation networks. In our future research, more complex network structures will be considered, link interaction in the cost function will be incorporated, and additional information delays will be taken into account that arise when travelers gather information about traffic conditions from other travelers or through intelligent transportation systems (ITS).

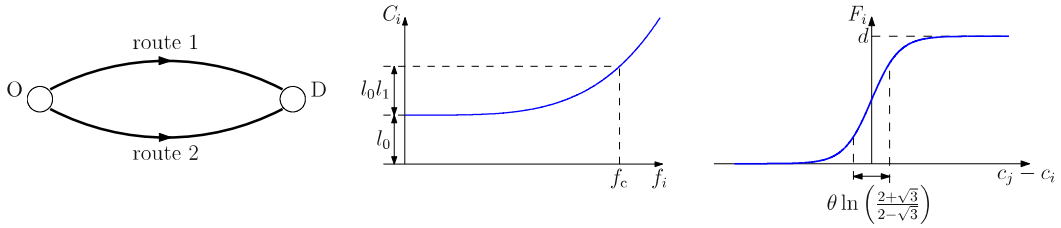

Fig. B.3. *Left*: a two-route traffic network with one origin–destination pair. *Middle*: nonlinear cost function given by Eq. (22). *Right*: the network loading function given by Eq. (23).

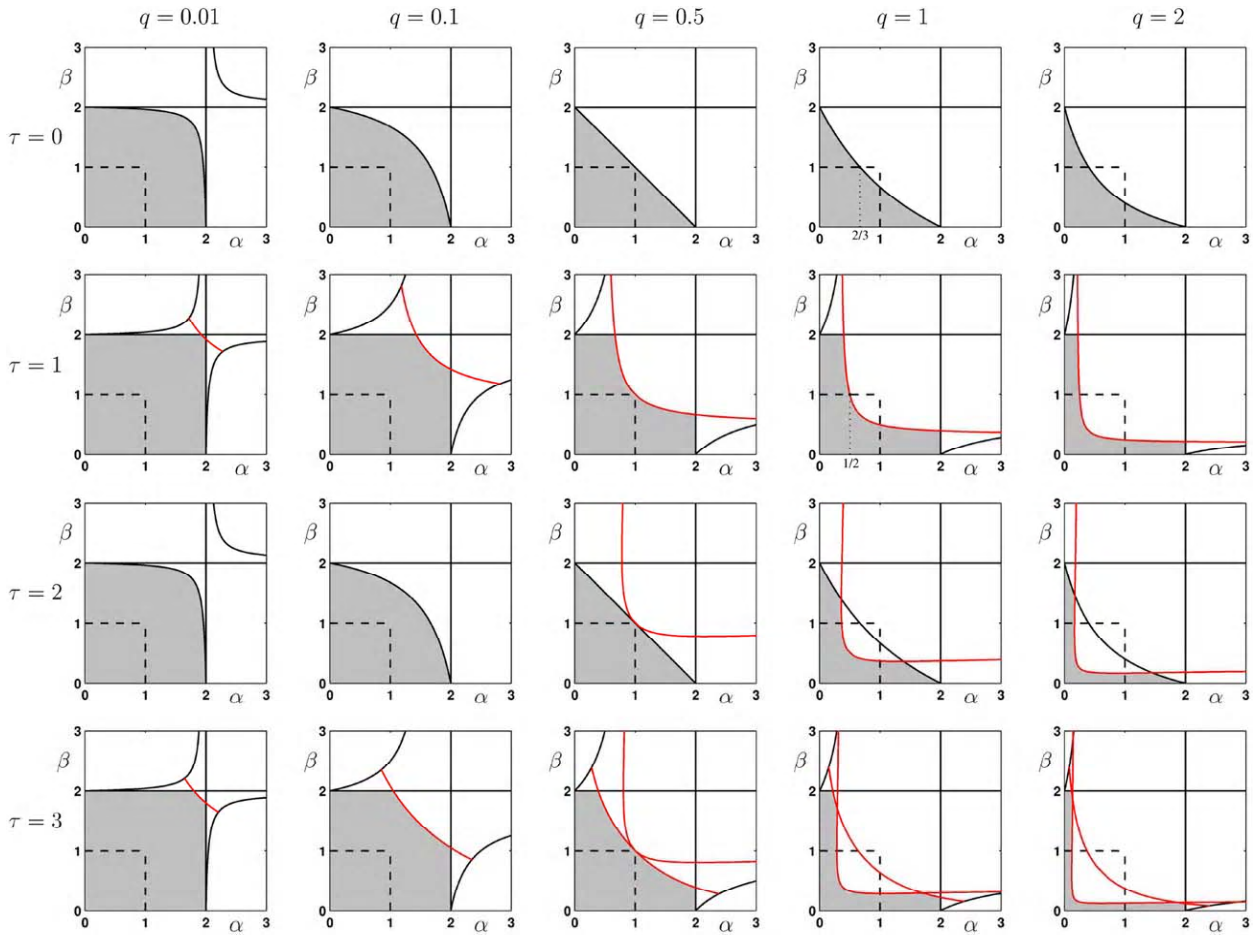

Fig. B.4. Linear stability charts depicting the stability curves in the (α, β) parameter plane for different values of parameters q and τ. For each panel the shaded domain corresponds to linearly stable equilibrium and the physically relevant domain is indicated by a dashed frame. The stable region is bounded by flip (black) and Neimark–Sacker (red) bifurcation curves. (For interpretation of the references to color in this figure legend, the reader is referred to the web version of this article.)

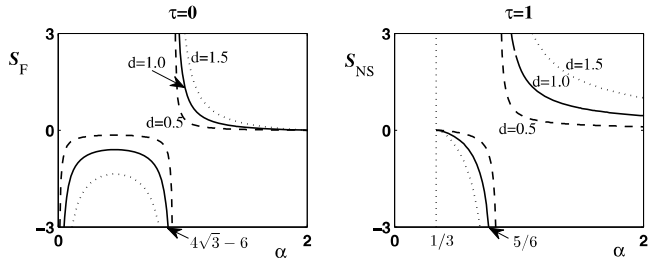

Fig. B.5. The coefficients (34) and (39) are plotted as a function of α for different demand values d as indicated when $q = 1$. The left and right panels visualize the criticality of flip and Neimark–Sacker bifurcations, respectively. The bifurcations are subcritical for $S < 0$ and supercritical for $S > 0$.

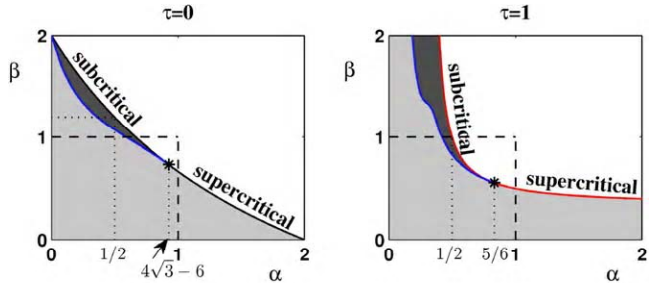

Fig. B.6. Two dimensional bifurcation diagrams showing the global dynamics for flip (left) and Neimark–Sacker (right) bifurcations when $q = 1$ and $d = 1$. The change of criticality is indicated by a star that corresponds to the formulae (35) and (40) and the vertical asymptotes in Fig. B.5. White, light gray and dark gray regions correspond to unstable, globally stable and bistable dynamics for the fixed point. The blue curve shows the location of fold bifurcations along the branches of the oscillations, cf. Figs. B.7 and B.9. (For interpretation of the references to color in this figure legend, the reader is referred to the web version of this article.)

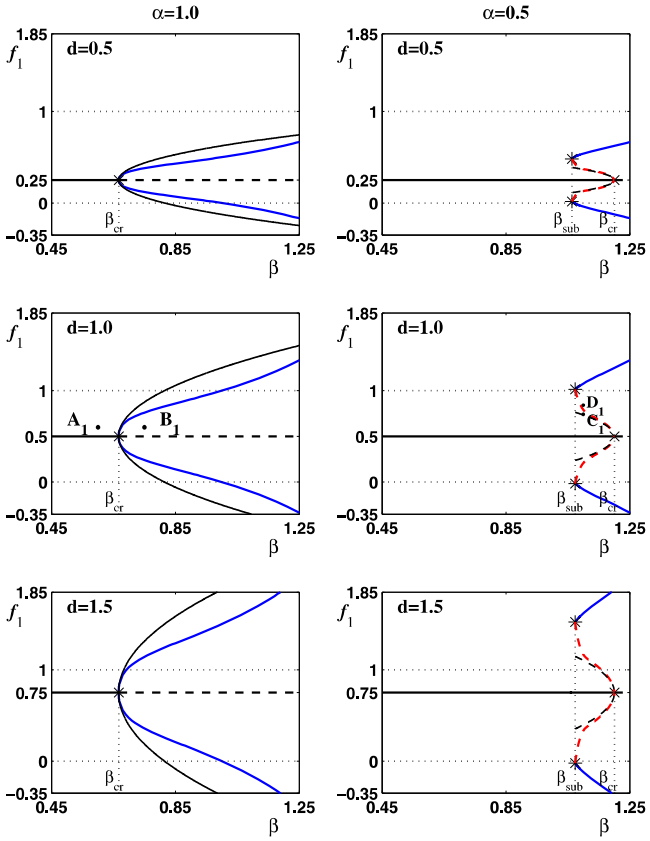

Fig. B.7. Super- and subcritical flip bifurcations shown on the left and right, respectively, for different values of α and d as indicated while $q = 1$ and $\tau = 0$. The horizontal line at $d/2$ represents the fixed point while the other curves represent the minima and maxima of oscillations. Stable and unstable solutions are shown as solid and dashed curves. Black curves are the results of analytical normal form calculations while colored curves are obtained by numerical continuation. The flip bifurcations are marked by crosses while fold bifurcations are marked by stars. (For interpretation of the references to color in this figure legend, the reader is referred to the web version of this article.)

Acknowledgments

We thank Harry Dankowicz for his help on the computation of invariant tori and we also acknowledge the discussions with Giuseppe Habib on normal form calculations. This work is funded by 973 Project (2012CB725400), the National Natural Science Foundation of China (Grant Nos. 71071012, 71271025, 71131001) and the Fundamental Research Funds for the Central Universities (Grant No. 2012JBM065).

Appendix A. Proof of Theorem 1

The eigenvalues of the matrix $\hat{\mathbf{J}}$ in (13) can be obtained by solving

$$\det\left[\lambda\hat{\mathbf{I}} - \hat{\mathbf{J}}\right] = \det\begin{bmatrix} (\lambda+\alpha-1)\mathbf{I} & 0 & 0 & 0 & \cdots & 0 & -\alpha\mathbf{J}_C \\ (\alpha-1)\beta\mathbf{J}_F & (\lambda+\beta-1)\mathbf{I} & 0 & 0 & \cdots & 0 & -\alpha\beta\mathbf{J}_F\mathbf{J}_C \\ 0 & -\mathbf{I} & \lambda\mathbf{I} & 0 & \cdots & 0 & 0 \\ 0 & 0 & -\mathbf{I} & \lambda\mathbf{I} & \cdots & 0 & 0 \\ \vdots & \vdots & 0 & -\mathbf{I} & \ddots & 0 & 0 \\ \vdots & \vdots & \vdots & \ddots & \ddots & \ddots & \vdots \\ 0 & 0 & 0 & 0 & \cdots & -\mathbf{I} & \lambda\mathbf{I} \end{bmatrix} = 0. \tag{A.1}$$

One may exploit that the determinant of the block matrix

$$\hat{\mathbf{P}} = \begin{bmatrix} \mathbf{A} & \mathbf{B} \\ \mathbf{C} & \mathbf{D} \end{bmatrix} \tag{A.2}$$

can be calculated as

$$\det[\hat{\mathbf{P}}] = \det[\mathbf{D}]\det[\mathbf{A} - \mathbf{B}\mathbf{D}^{-1}\mathbf{C}], \tag{A.3}$$

if $\mathbf{D}$ is invertible. Partitioning the matrix in (A.1) such that $\mathbf{A}$ is chosen to be the $2n_A \times 2n_A$ matrix at the top left corner and recognizing that

$$\mathbf{D}^{-1} = \begin{bmatrix} \frac{1}{\lambda}\mathbf{I} & & & & 0 \\ \frac{1}{\lambda^2}\mathbf{I} & \frac{1}{\lambda}\mathbf{I} & & & \\ \frac{1}{\lambda^3}\mathbf{I} & \frac{1}{\lambda^2}\mathbf{I} & \frac{1}{\lambda}\mathbf{I} & & \\ \vdots & \ddots & \ddots & \ddots & \\ \frac{1}{\lambda^\tau}\mathbf{I} & \cdots & \frac{1}{\lambda^3}\mathbf{I} & \frac{1}{\lambda^2}\mathbf{I} & \frac{1}{\lambda}\mathbf{I} \end{bmatrix}, \tag{A.4}$$

formula (14) can be derived.

If $\mathbf{J}_F\mathbf{J}_C$ is diagonalizable then there exist n_A linearly independent (n_A-dimensional) eigenvectors that can be used as the columns of a transformation matrix $\mathbf{T}$ to obtain

$$\mathrm{diag}[\gamma_i] = \mathbf{T}^{-1}\mathbf{J}_F\mathbf{J}_C\mathbf{T}, \tag{A.5}$$

where γ_i is the ith eigenvalue of $\mathbf{J}_F\mathbf{J}_C$. Using this and the identity

$$\det[\mathbf{ABC}] = \det[\mathbf{A}]\det[\mathbf{B}]\det[\mathbf{C}], \tag{A.6}$$

one can derive (15) from (14). We remark that if $\mathbf{J}_F\mathbf{J}_C$ is not diagonalizable, then the above transformation leads to a Jordan normal form which still allows a calculation of eigenvalues but the algebraic calculations become more involved.

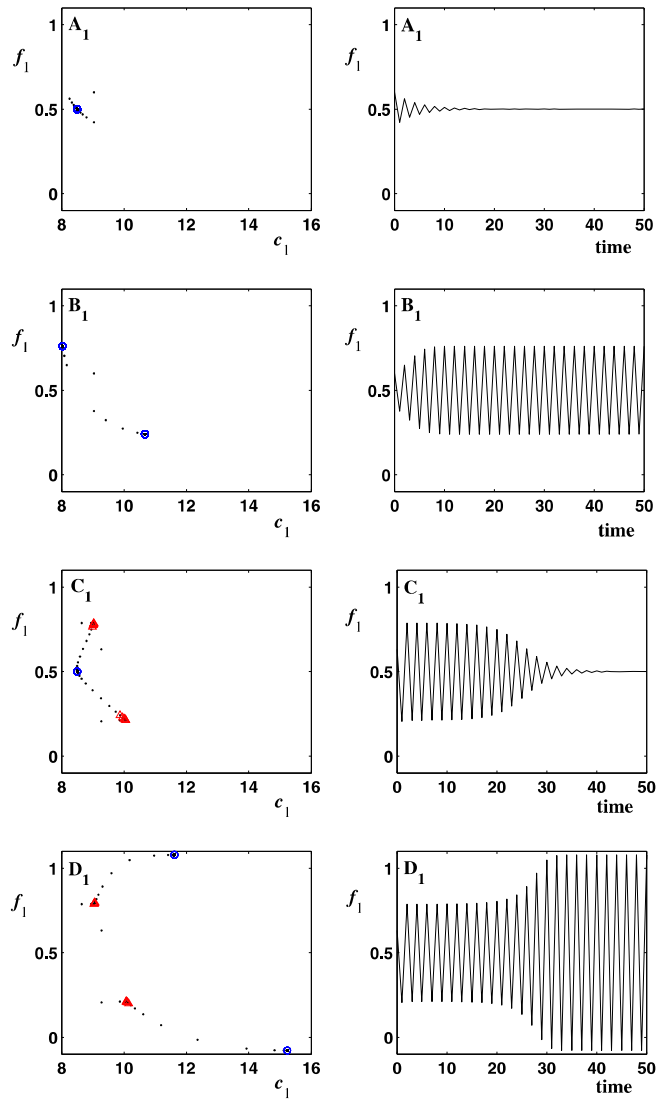

Fig. B.8. Simulation results corresponding to the points A_1, B_1, C_1, D_1 marked in the middle panels of Fig. B.7. Trajectories are shown in the space (f_1, c_1) on the left where stable and unstable invariant orbits are marked as blue circles and red triangles, respectively. The time evolution of f_1 is shown on the right. (For interpretation of the references to color in this figure legend, the reader is referred to the web version of this article.)

Appendix B. Normal form calculations

As mentioned in the main text, using a set of nonlinear coordinate transformations one may derive low-dimensional normal form equations that govern the dynamics of the high-dimensional system. Here we provide some insight into how this applies to the two-route transportation network ($n_A = n_w = 2$) discussed in Section 5; see [41] for more technical details. In this case the subspace defined by the flow conservation constraint $f_1 + f_2 = d$ is invariant. Moreover, the network loading function (23) only depends on the cost difference $c_1 - c_2$. These allow us to reduce the dimension of the state space by $2 + \tau$ before performing the normal form calculations.

Thus, for $\tau = 0$ the dimension of the system reduces to $(2 + \tau) \times (n_A - 1) = 2$ and this has to be projected to a one-dimensional invariant manifold corresponding to the flip bifurcation. This yields the normal form

$$\xi_{t+1} = \lambda(\beta)\xi_t - \delta(\beta)\xi_t^3, \tag{B.1}$$

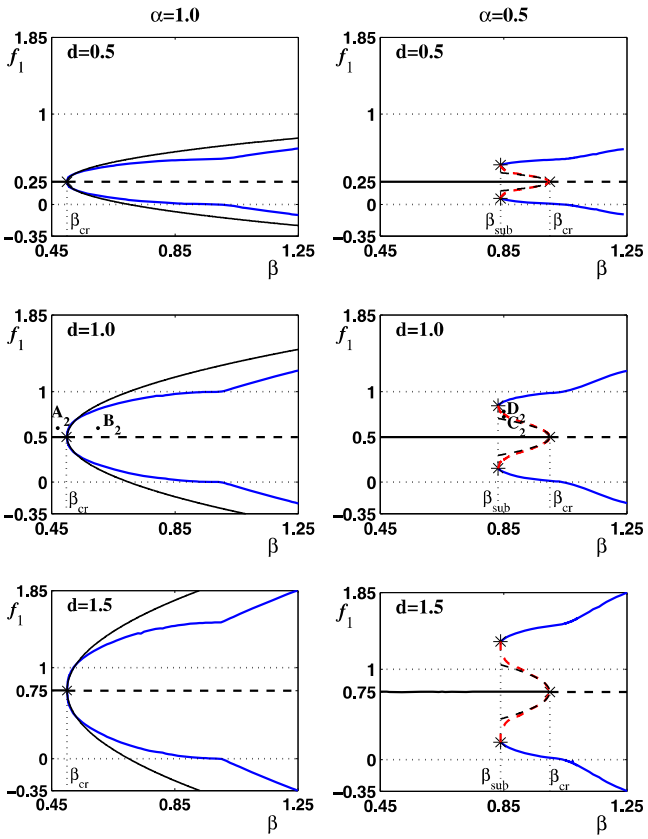

Fig. B.9. Super- and subcritical Neimark–Sacker bifurcations shown on the left and right, respectively, for different values of α and d as indicated while $q = 1$ and $\tau = 1$. The same notation is used as in Fig. B.7 except that crosses indicate Neimark–Sacker bifurcations. (For interpretation of the references to color in this figure legend, the reader is referred to the web version of this article.)

where $\xi_t \in \mathbb{R}$ and $\beta \in \mathbb{R}$ is the bifurcation parameter so that $\lambda(\beta_{cr}) = -1$, i.e., the linear part gives the eigenvalues -1 at the critical case $\beta = \beta_{cr}$. In the vicinity of the bifurcation the oscillations can be written as

$$\xi_t = \sqrt{-\frac{\frac{d|\lambda|}{d\beta}\Big|_{\beta_{cr}}}{\delta(\beta_{cr})}(\beta - \beta_{cr})} \cdot (-1)^t. \tag{B.2}$$

In this formula $\frac{d|\lambda|}{d\beta}|_{\beta_{cr}}$ determines whether stability is lost or gained when increasing β through β_{cr}. In our case

$$\frac{d|\lambda|}{d\beta}\Big|_{\beta_{cr}} = \frac{\left[2 - \alpha(1 - 2q)\right]^2}{4(1 - \alpha) + \alpha^2(1 + 2q)} > 0, \tag{B.3}$$

which means stability is lost when increasing β that corresponds to the linear stability charts in Fig. B.4. Moreover, the criticality of the bifurcation is given by $\delta(\beta_{cr})$ so that

$$\begin{cases} \delta(\beta_{cr}) > 0 \Rightarrow \text{ subcritical}, \\ \delta(\beta_{cr}) < 0 \Rightarrow \text{ supercritical}. \end{cases} \tag{B.4}$$

In our case

$$\delta(\beta_{cr}) = \frac{-16\alpha q\left[12(1 - \alpha) + \alpha^2(3 - 4q^2)\right]}{3d^2(\alpha - 2)\left[4(1 - \alpha) + \alpha^2(1 + 2q)\right]}. \tag{B.5}$$

That is, using (B.2), (B.3), (B.4), (B.5) and transforming the system back to the original variables one may derive (33), (34), (35).

For $\tau = 1$ the dimension of the system reduces to $(2 + \tau) \times (n_A - 1) = 3$ and this has to be projected to the two-dimensional

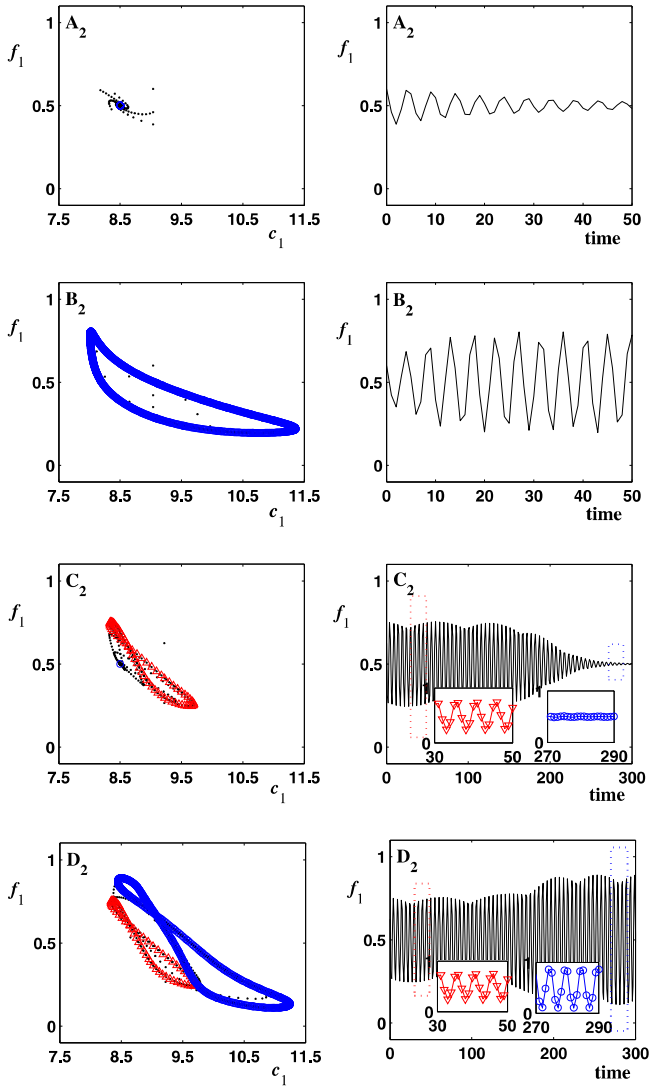

Fig. B.10. Simulation results corresponding to the points A_2, B_2, C_2, D_2 marked in the middle panels of Fig. B.9. Trajectories are shown in the space (f_1, c_1) on the left while the time evolution of f_1 is shown on the right. The same notation is used as in Fig. B.8.

invariant manifold corresponding to the Neimark–Sacker bifurcation in order to obtain the normal form

$$\begin{bmatrix}\xi_{t+1}\\ \eta_{t+1}\end{bmatrix} = r(\beta)\begin{bmatrix}\cos\psi(\beta) & \sin\psi(\beta)\\ -\sin\psi(\beta) & \cos\psi(\beta)\end{bmatrix}\begin{bmatrix}\xi_t\\ \eta_t\end{bmatrix} + (\xi_t^2+\eta_t^2)\begin{bmatrix}\cos\psi(\beta) & \sin\psi(\beta)\\ -\sin\psi(\beta) & \cos\psi(\beta)\end{bmatrix} \times \begin{bmatrix}\delta(\beta) & \kappa(\beta)\\ -\kappa(\beta) & \delta(\beta)\end{bmatrix}\begin{bmatrix}\xi_t\\ \eta_t\end{bmatrix}, \tag{B.6}$$

where $\xi_t, \eta_t \in \mathbb{R}$, $r(\beta_{cr}) = 1$, and $\psi(\beta_{cr}) = \phi \in (0, \pi)$, i.e., the linear part gives the eigenvalues $\psi(\beta_{cr}) = \exp(\pm i\phi)$ at $\beta = \beta_{cr}$. Close to the bifurcation the oscillations can be written as

$$\begin{bmatrix}\xi_t\\ \eta_t\end{bmatrix} = \sqrt{-\frac{\frac{d|\lambda|}{d\beta}\Big|_{\beta_{cr}}}{\delta(\beta_{cr})}(\beta-\beta_{cr})}\cdot\begin{bmatrix}\cos\phi t\\ -\sin\phi t\end{bmatrix}, \tag{B.7}$$

where again $\frac{d|\lambda|}{d\beta}|_{\beta_{cr}}$ determines on which side of β_{cr} the system is stable while $\delta(\beta_{cr})$ gives the criticality as in (B.4). In our case

$$\frac{d|\lambda|}{d\beta}\Big|_{\beta_{cr}} = \frac{\alpha(1+2q)-1}{2} > 0, \tag{B.8}$$

and

$$\delta(\beta_{cr}) = -\frac{\alpha^2 q\left[2\alpha q(1+2q)-2q-3\right]}{d^2\left[\alpha(1+2q)-1\right]}. \tag{B.9}$$

Thus, (B.7), (B.8), (B.4), (B.9) yields (38), (39), (40) for the physical variables.

References

[1] J.G. Wardrop, Some theoretical aspects of road traffic research, Proc. Inst. Civ. Eng. 1 (1952) 325–378.
[2] R. Roughgarden, E. Tardos, How bad is selfish routing? J. ACM 49 (2) (2002) 236–259.
[3] C.F. Daganzo, Y. Sheffi, On stochastic models of traffic assignment, Transp. Sci. 11 (3) (1977) 253–274.
[4] J.L. Horowitz, The stability of stochastic equilibrium in a two-link transportation network, Transp. Res. B 18 (1) (1984) 13–28.
[5] X. He, X. Guo, H.X. Liu, A link-based day-to-day traffic assignment model, Transp. Res. B 44 (4) (2010) 597–608.
[6] M.J. Smith, The stability of a dynamic model of traffic assignment—an application of a method of Lyapunov, Transp. Sci. 18 (3) (1984) 245–252.
[7] T.L. Friesz, D. Bernstein, N.J. Mehta, R.L. Tobin, S. Ganjalizadeh, Day-to-day dynamic network disequilibria and idealized traveler information-systems, Oper. Res. 42 (6) (1994) 1120–1136.
[8] D. Zhang, A. Nagurney, On the local and global stability of a travel route choice adjustment process, Transp. Res. B 30 (4) (1996) 245–262.
[9] D.P. Watling, M.L. Hazelton, The dynamics and equilibria of day-to-day assignment models, Netw. Spat. Econ. 3 (3) (2003) 349–370.
[10] A. Nagurney, D. Zhang, Projected dynamical systems in the formulation, stability analysis, and computation of fixed-demand traffic network equilibria, Transp. Sci. 31 (2) (1997) 147–158.
[11] X. He, H.X. Liu, Modeling the day-to-day traffic evolution process after an unexpected network disruption, Transp. Res. B 46 (1) (2012) 50–71.
[12] J. Bie, H.K. Lo, Stability and attraction domains of traffic equilibria in a day-to-day dynamical system formulation, Transp. Res. B 44 (1) (2010) 90–107.
[13] E.A. Cascetta, Stochastic process approach to the analysis of temporal dynamics in transportation networks, Transp. Res. B 23 (1) (1989) 1–17.
[14] M.L. Hazelton, D.P. Watling, Computation of equilibrium distributions of Markov traffic assignment models, Transp. Sci. 38 (3) (2004) 331–342.
[15] G.E. Cantarella, E. Cascetta, Dynamic processes and equilibrium in transportation networks: towards a unifying theory, Transp. Sci. 29 (4) (1995) 305–329.
[16] D. Watling, Stability of the stochastic equilibrium assignment problem: a dynamical systems approach, Transp. Sci. 33 (4) (1999) 281–312.
[17] G.E. Cantarella, Day-to-day dynamic models for intelligent transportation systems design and appraisal, Transp. Res. C 29 (2013) 117–130.
[18] R.M. Pendyala, E.I. Pas, Multi-day and multi-period data for travel demand analysis and modeling, in: TRB Transportation Research Circular E-C008: Transportation Surveys: Raising the Standard, 2012.
[19] J.O. Huff, S. Hanson, Repetition and variability in urban travel, Geogr. Anal. 18 (2) (1986) 97–113.
[20] J. Huff, S. Hanson, Classification issues in the analysis of complex travel behavior, Transportation 13 (3) (1986) 271–293.
[21] J.O. Huff, S. Hanson, Systematic variability in repetitious travel, Transportation 15 (1–2) (1988) 111–135.
[22] J.O. Huff, S. Hanson, Measurement of habitual behavior: examining systematic variability in repetitive travel, in: P. Jones (Ed.), Developments in Dynamic and Activity-Based Approaches to Travel Analysis, Gower Publishing Co., 1990.
[23] C. Raux, T.-Y. Ma, E. Cornelis, Variability Versus Stability in Daily Travel and Activity Behavior. the Case of One Week Travel Diary, Tech. Rep., HAL, 2011. http://econpapers.repec.org/paper/halwpaper/halshs-00612610.htm.
[24] P. Stopher, Y. Zhang, Is travel behavior repetitive from day to day? in: ATRF 2010: 33rd Australian Transport Research Forum, 2010. www.atrf.info/papers/2010/2010_Stopher_Zhang_B.pdf.
[25] E. Cascetta, G.E. Cantarella, Modelling dynamics in transportation networks: state of the art and future developments, Simul. Pract. Theory I (1993) 65–91.
[26] G.E. Cantarella, P. Veloná, Stability analysis of equilibrium patterns in a transportation network, in: Proceedings of the European Transport Conference, 2003.
[27] G. Orosz, R.E. Wilson, G. Stépán, Traffic jams: dynamics and control, Phil. Trans. R. Soc. A 368 (1928) (2010) 4455–4479.
[28] G. Orosz, G. Stépán, Subcritical Hopf bifurcations in a car-following model with reaction-time delay, Proc. R. Soc. A 462 (2073) (2006) 2643–2670.
[29] G. Orosz, R.E. Wilson, R. Szalai, G. Stépán, Exciting traffic jams: Nonlinear phenomena behind traffic jam formation on highways, Phys. Rev. E 80 (4) (2009) 046205.
[30] X. Zhao, Z. Gao, The stability analysis of the full velocity and acceleration velocity model, Physica A 375 (2) (2007) 679–686.
[31] M.M. Gomez, G. Orosz, R.M. Murray, Stability of discrete time systems with stochastically delayed feedback, in: Proceeding of the European Control Conference, 2013, pp. 2609–2614.
[32] Bureau of Public Roads, Traffic Assignment Manual, Tech. Rep., US Department of Commerce, Washington, DC, 1964.
[33] C.M. Penchina, Minimal revenue tolls: price stability for networks with BPR cost function, Open Transp. J. 3 (2009) 87–92.

[34] Y. Sheffi, Urban Transportation Networks: Equilibrium Analysis with Mathematical Programming Method, Prentice Hall, 1985.
[35] G.E. Cantarella, A general fixed-point approach to multi-mode multi-user equilibrium assignment with elastic demand, Transp. Sci. 31 (2) (1997) 107–128.
[36] J. Guckenheimer, P. Holmes, Nonlinear Oscillations, Dynamical Systems, and Bifurcations of Vector Fields, in: Applied Mathematical Sciences, vol. 42, Springer, 1983.
[37] Y.A. Kuznetsov, Elements of Applied Bifurcation Theory, third ed., in: Applied Mathematical Sciences, vol. 112, Springer, 2004.
[38] G. Habib, G. Rega, G. Stépán, Nonlinear bifurcation analysis of a single-DoF model of a robotic arm subject to digital position control, Int. J. Solids Struct. 8 (1) (2013) 011009.
[39] W. Govaerts, Y.A. Kuznetsov, V. De Witte, A. Dhooge, H.G.E. Meijer, W. Mestrom, A.M. Riet, B. Sautois, MATCONT and CL_MATCONT: Continuation Toolboxes in MATLAB, Tech. Rep., 2011. http://www.matcont.ugent.be/.
[40] H. Dankowicz, G. Thakur, A Newton method for locating invariant tori of maps, Int. J. Bifurcation Chaos 16 (5) (2006) 1491–1503.
[41] G. Orosz, X. Zhao, Normal form calculations for day-to-day traffic dynamics, in: Proceedings of the 8th European Nonlinear Dynamics Conference, 2014.